Interfacial Polymer Engineered Field Effect Transistor Biosensors for Rapid and Efficient Identification of SARS-CoV-2 N Antigen

Qiumin Peng,[‡,a] Wanting Huang,[‡,a] Duo Chen,[‡,a] Zhipeng Gao,[a] Yanbing Yang,*[,a] and Quan Yuan*[,a,b]

[a] *College of Chemistry and Molecular Sciences, Key Laboratory of Biomedical Polymers of Ministry of Education, Institute of Molecular Medicine, Renmin Hospital of Wuhan University, School of Microelectronics, Wuhan University, Wuhan, Hubei 430072, China*
[b] *Molecular Science and Biomedicine Laboratory (MBL), State Key Laboratory of Chemo/Biosensing and Chemometrics, College of Chemistry and Chemical Engineering, Hunan University, Changsha, Hunan 410082, China*

Keywords

Field effect transistor | Debye screening effect | Biosensing | Interfacial engineering | Epidemic screening

Comprehensive Summary
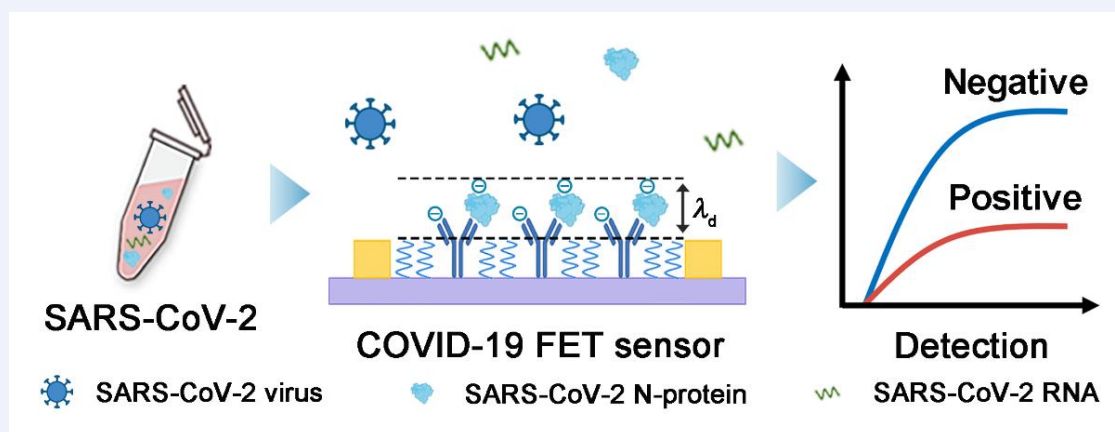
With the advantages of high sensitivity, rapid response, label-free, and simple operation, field effect transistor biosensors have shown promising application prospects in large-scale pathogen screening. However, in practical biological fluids with relatively high ionic strength, such as saliva and serum, the Debye screening effect will weaken the interaction between FET biosensors and target bio-molecules, thereby affecting the sensing sensitivity and accuracy. Herein, an interfacial polymer-engineered field effect transistor (IPE FET) biosensor was developed for the efficient identification of SARS-CoV-2 N antigens in saliva samples. The inclusion of a polymer layer shortens the distance between target molecules and the electrode interface, which effectively overcomes the limitation of Debye screening. The constructed IPE FET biosensors exhibit high sensitivity and anti-fouling capability, achieving efficient detection of SARS-CoV-2 N antigen in saliva within 5 min with a detection limit of 4.6 fg·mL^{-1}. In a cohort of 35 simulated throat swab samples of SARS-CoV-2 N antigen, IPE FET exhibits an identification accuracy of up to 97.1%, with predictive sensitivity and specificity of 96.0% and 100.0%, respectively. The excellent performance of IPE FET not only provides a strategy to design efficient detection platforms but also suggests a pathway to realize rapid and scalable epidemic screening.

*E-mail: yuanquan@whu.edu.cn
          yangyanbing@whu.edu.cn
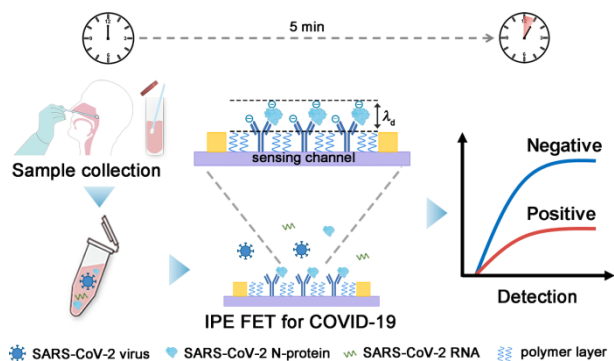[‡] These authors contributed equally to this work.

Background and Originality Content

The Coronavirus disease 19 (COVID-19) pandemic caused by severe acute respiratory syndrome coronavirus 2 (SARS-CoV-2) and its variants poses a great threat to public health worldwide.[1-3] Developing high sensitivity assay for the fast detection and quantification of SARS-CoV-2 relevant nucleic acids, antigens, and antibodies is highly required to suppress pandemic spreading and assist vaccine efficiency assessment.[4-6] During the infection process, SARS-CoV-2 relevant nucleic acids and antigens were released into the blood within 24 h, and antibodies could only be detected after the appearance of immune response or the onset of clinical symptoms.[7-8] Compared to nucleic acids detection which requires complicated and timely nucleic acids amplification procedures, trained personnel operation, and a centralized laboratory, antigen detection offers a fast and simple approach for efficient pandemic screening.[9-10] SARS-CoV-2 mainly includes 4 types of antigens: nucleocapsid (N), spike (S), membrane (M), and envelop (E) proteins. Among them, the N protein dominates the viral replication process and is less susceptive to mutation.[11] Also, N protein is highly expressed during the SARS-CoV-2 replication process, making it a suitable target for fast and reliable COVID-19 screening.[12-14] Currently, the established antigen detection method mainly relies on lateral-flow immunoassays due to their simple and easy operation characteristics.[15-17] However, the practical point-of-care application of lateral-flow immunoassay is hindered by its relatively low sensitivity and specificity which often leads to false-positive or false-negative results.[18-19]

Field-effect transistor (FET) biosensors with intrinsic signal amplification capability could directly convert trace biomolecule information into a readable electrical signal, endowing its high sensitivity characteristic.[20-23] Particularly, the response time of FET biosensors for target detection reaches as low as a few seconds and the dimension of FET biosensors could be miniatured to a portable format, promising the potential of FET biosensors in real-time and point-of-care N antigen monitoring.[24-26] The sensing principle of FET biosensors relies on the change in charge carriers at the biosensing interface upon the recognition of charged target biomolecules.[27-28] Yet, in practical biological environments such as saliva with relatively high ionic strength, the biosensing interface and charged biomolecules would be severely screened by oppositely charged ions through electrostatic interaction.[29-30] The extent of screening, called the Debye screening effect, would severely shorten the effective sensing distance characterized by Debye length, thus weakening the interaction between FET biosensors and target N antigens.[31]

To address these limitations, we developed an interfacial polymer-engineered field-effect transistor (IPE FET) biosensor to efficiently identify SARS-CoV-2 N antigen in untreated saliva samples (Scheme 1). The inclusion of a polymer layer above the sensing channel overcomes the limitation of Debye screening effect, resulting in increased interaction between the N antigen target and recognition molecules. The specific binding between N antigen and recognition molecules was identified and amplified by the FET biosensor and converted into readable electrical signals within 5 min. The uniform distributed recognition molecules on the FET surface endow the biosensors with the capability to reliably detect N antigen with an extremely low detection limit of 4.6 fg·mL^{-1}. The FET biosensor exhibits a broader linear range and higher sensitivity than Enzyme-Linked Immunosorbent Assay (ELISA). Importantly, the developed FET biosensor delivers a sensitivity of 96.0% and specificity of 100.0% after analyzing a cohort of 25 SARS-CoV-2 positive saliva samples and 10 negative saliva samples. Our developed IPE FET biosensor provides an efficient strategy for designing ultrasensitive, timely, and reliable biosensors for pandemic screening.

Results and Discussion

Fabrication and characterization of IGZO FETs

An 8-channel transistor array was prepared with 500 μm × 1400 μm IGZO semiconductor layers on each channel (Figure S1). Cr/Au electrodes were firstly grown on a silicon wafer substrate by thermal vaporizer, and a ceramic target ($In_2O_3 : Ga_2O_3 : ZnO = 1 : 1 : 1$) was used to deposit IGZO channel layers by magnetron sputtering with the aid of a metal mask. Figure S1 shows that the electrodes on IGZO FET array are clearly outlined, and the prepared IGZO channel materials are uniform in color and size. The SEM image clearly showed the homogeneous and smooth surface of the IGZO layer with a thickness of about 20 nm (Figure 1a).

In order to determine the capability of the prepared transistor arrays for constructing high-performance biosensors, the electrical properties of IGZO FETs were first investigated. With the substrate Si as the gate and the SiO$_2$ layer as the gate dielectric, we test the transfer characteristic curve of IGZO FETs in the atmospheric environment. As shown in Figure 1b, the IGZO FET shows typical N-type transistor transfer characteristics with an on-state current of 40 μA, a current on/off ratio of 1.2×10^6, and carrier mobility of 12.4 cm^2·V^{-1}·s^{-1}. The output characteristic curve of the solution-gated IGZO FET was obtained by holding gate voltage (V_g) at a constant value and linearly scanning source–drain voltage (V_d) (Figure 1b). The drain current (I_d) increases with V_d, passing through the original point and having a linear relationship,

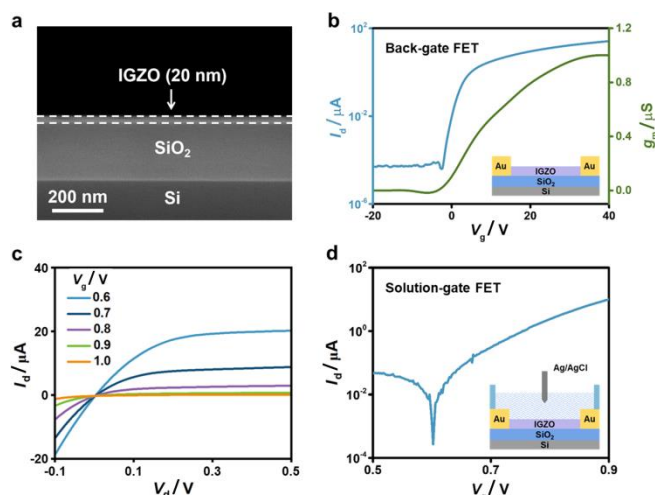**Scheme 1** IPE FET biosensors for the rapid and precise identification of SARS-CoV-2 N antigen

Figure 1 Fabrication and electrical performance of IGZO FETs. (a) Cross-section SEM image of IGZO FETs. The thickness of IGZO channel is about 20 nm. (b) Transfer characteristic and transconductance of IGZO FET at V_d = 2 V. Inset is the structure diagram of back-gate IGZO FETs. (c) Output characteristic curves of solution-gated IGZO FET device with V_g ranging from 0.6 to 1.0 V in steps of 0.1 V. (d) Transfer characteristic curve of a solution-gated IGZO FET device at V_d = 0.2 V. Inset is the structure diagram of solution-gate IGZO FETs.

indicating that an ohmic contact is formed between the source-drain electrode and the channel material. The output characteristic curves exhibit similar variation under different gate voltages, indicating that V_g can effectively regulate the electrical properties of channel materials (Figure 1c). Additionally, the transfer characteristis of IGZO FET were well maintained under liquid-gated voltage (Figure 1d), and the 8 sensing channels exhibit excellent repeatability (Figure S2), promising the extraordinary performance of IGZO FET in biosensing. The above results demonstrate the excellent electrical properties of IGZO FET arrays, which guarantee their ability to construct high-performance biosensors.

Construction and optimization of IPE FETs

Due to electrostatic interactions, charged proteins in a biological buffer solution are surrounded by inversely charged ions, reducing the effective charge of biomolecules. The above effect is called Debye shielding, and the control distance of its effective electric field is called Debye length (λ_D):

$$\lambda_D = \sqrt{\frac{\varepsilon k_B T}{2 N_A q^2 I}} \tag{1}$$

where k_B, T, and N_A represent Boltzmann's constant, temperature, and Avogadro number, respectively. I is the ionic strength of the solution, and q is the electron charge. The effective electrical field of FET biosensors could only be controlled within λ_D. For typical biological samples such as blood, urine, and saliva with high ionic strength, the detection of biomolecules with relatively large sizes such as antigens and antibodies would be severely influenced by the Debye screening effect. In order to overcome the above limitation and achieve highly sensitive antigen detection, we engineered the interface of FET biosensors to shorten the distance between the target N antigen and the IGZO sensing channel through interfacial polymer engineering (Figure 2a). Figure S3 shows the preparation process of IPE FET biosensors. Specifically, the antibody of SARS-CoV-2 N antigen was firstly immobilized on the amino-modified IGZO surface *via* glutaraldehyde crosslinker molecules. Subsequently, two types of polymers including polydopamine (PDA) and polypyrrole (PPy) were functionalized on the surface of IGZO with solution polymerization and electrodeposition to obtain PDA-IGZO FET and PPy-IGZO FET biosensors. The

absorption peaks corresponding to amide bonds at 1530 cm^{-1} and 1650 cm^{-1} were observed in the attenuated total reflection Fourier transform infrared spectroscopy (ATR-FTIR), indicating that the antibody of SARS-CoV-2 N antigen was successfully immobilized on the surface of IPE FET.[32-33] The corresponding PDA absorption peaks at 1494 cm^{-1} and 1274 cm^{-1}, and the PPy absorption peaks at 957 cm^{-1}, 1035 cm^{-1}, and 1209 cm^{-1} confirmed the successful modification of PDA and PPy, respectively (Figure 2b).[34-35] The presence of characteristic peaks of C 1s (286.6 eV), N 1s (399.9 eV), and S 2p (162.4 eV) in the X-ray photoelectron spectroscopy (XPS) further demonstrates the successful construction of IPE FET biosensors (Figure S4).[27] The transfer characteristic curves of PDA-IGZO FET and PPy-IGZO FET indicate that the modification of polymer does not affect the electrical properties of IGZO FETs (Figure S5).

In order to evaluate the performance of the IPE FET biosensors, real-time dynamic measurements were carried out. We successively added interfering molecules (1 ng·mL^{-1} BSA) and target proteins (1 pg·mL^{-1} N antigen) to the IGZO FET, PDA-IGZO FET, and PPy-IGZO FET biosensors, and recorded the changes in I_d over time, respectively (Figure 2c). The percentage ratio of the change in I_d (ΔI) to the initial current magnitude (I_o) was expressed as the current response ($\Delta I/I_o$). As shown in Figure 2d, IPE FET biosensors show significantly higher current responses to the target N antigen compared to IGZO FET biosensors. The current response difference of FET biosensors with and without polymer functionalization was more pronounced at higher concentrations of PBS solution (Figure 2e). The reason lies in the fact that the modified polymer layer fills the gap between the antibody-binding fraction and the sensing channel, thus narrowing the distance between target N antigen and FET surface and allowing more charges on the N antigen located within the Debye length. A decreased current response was observed when the polymer deposition layer was increased (Figure S6). This phenomenon may be due to that the binding fraction of antibody was covered and the binding ability of the sensing interface to the N antigen was diminished. In addition, the current response of FET biosensors to interfering molecules was reduced after polymer modification (Figure 2d). As shown in Figure S7 and Figure S8, after 4 h immersion in the single-stranded DNA solution labeled by FAM and the
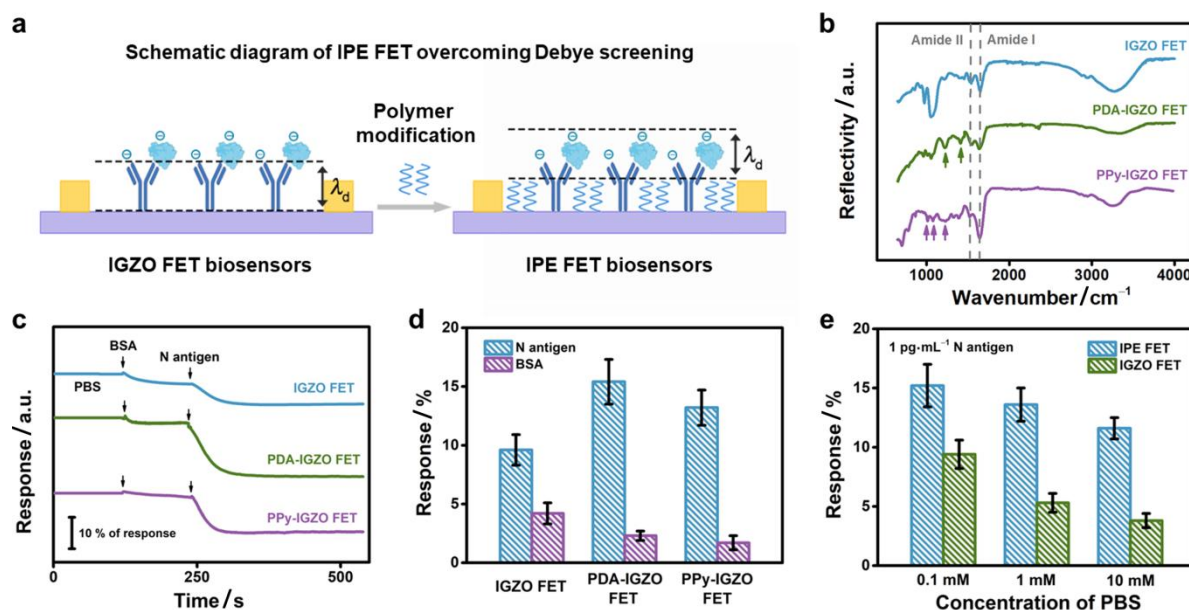
Figure 2 Preparation and characterization of IPE FETs. (a) Schematic diagram to illustrate the influence of polymer modification layer to overcome the Debye screening. (b) The FTIR spectra of IGZO FET, PDA-IGZO FET, and PPy-IGZO FET. Characteristic absorption peaks are marked on the spectra. (c) Real-time response of the FET biosensors toward BSA and SARS-CoV-2 N antigen with and without polymer modification. (d) Comparison of the current responses of FET biosensors toward BSA and SARS-CoV-2 N antigen with and without polymer modification. (e) Current responses of IGZO FETs and PDA-IGZO FETs towards target N antigen under different ionic strengths. Data in d and e are reported as mean ± S.D. (n = 3).

bacterial suspension stained with DAPI, respectively, the adsorption of biomolecules/cells on IPE FET was significantly less than that on IGZO FET. The above results indicate that interfacial polymer modification can improve the sensing sensitivity and antifouling ability of FET biosensors.

Detection of SARS-CoV-2 N antigen by IPE FET biosensors

To investigate the detection performance of IPE FET, we measured the transfer characteristic curves of the IPE FET biosensors toward various concentrations of SARS-CoV-2 N antigen at optimized antibody modification concentrations and antibody incubation times (Figure S9). As shown in Figure 3a, the I_d of the PDA-IGZO FET decreases continuously with the increase of SARS-CoV-2 N antigen concentration. The current variation is due to the accumulation of negative surface charge in the n-type IGZO channel upon the binding of negatively charged SARS-CoV-2 N antigen. Similar variations were observed in both IGZO FETs and PPy-IGZO FETs (Figure S10 and Figure S11). The current response ($\Delta I/I_o$) was utilized to evaluate the detection performance of the FET biosensors. As shown in Figure 3b, PDA-IGZO FETs produced a 13.6% current response to SARS-CoV-2 N antigen with concentrations as low as 0.01 pg·mL^{-1}, significantly higher than the current response without the target. The current response increased linearly as the SARS-CoV-2 N antigen concentration increased from 0.01 pg·mL^{-1} to 100 pg·mL^{-1}. Compared with IGZO FETs, IPE FETs exhibit a significantly improved current response with a lower detection limit and a wider linear detection range. Based on the calibration curve, the detection limits of IGZO FETs, PDA-IGZO FETs, and PPy-IGZO FETs were calculated as 0.65 pg·mL^{-1}, 0.0046 pg·mL^{-1}, and 0.0067 pg·mL^{-1}, respectively (S/N = 3).

For a further step, we evaluated the specificity and stability of IPE FETs. In view of the highly similar antigen structure of coronaviruses, N antigens of SARS-CoV and MERS-CoV were selected to evaluate the specificity of PDA-IGZO FETs. As shown in Figure 3c, PDA-IGZO FET produced a current response of 43.2% toward 1 pg·mL^{-1} of SARS-CoV-2 N antigen, much higher than the response to MERS-CoV N antigen (8.6%). However, a 23.1% current response was produced toward 1 pg·mL^{-1} SARS-CoV N antigen by PDA-IGZO FETs due to a certain degree of binding between

SARS-CoV N antigen and SARS-CoV-2 N antibody. We then immersed IGZO FET and IPE FET in 1 ng·mL^{-1} BSA solution for 4 h and measured the current response of the FET biosensors, respectively. As shown in Figure 3d and Figure S12, the current responses of PDA-IGZO FETs and PPy-IGZO FETs remained consistent before and after BSA treatment, while the current responses of IGZO FETs were significantly reduced. For 1 pg·mL^{-1} SARS-CoV-2 N antigen, PDA-IGZO FETs and PPy-IGZO FETs maintained 92.5% and 90.6% current response after treatment with BSA, while the IGZO FETs reduced to 63.7% of their pre-treatment response value. In comparison, PDA-IGZO FETs showed superior detection performance compared with PPy-IGZO FETs, and this phenomenon may be attributed to the uniform PDA layer alleviating the biofouling. In addition, the IPE FET can maintain its sensing performance at 4 °C for up to 7 d (Figure S13). These results indicate that the IPE FET exhibits higher sensitivity and a better anti-biofouling ability for the detection of SARS-CoV-2 N antigen, which is conducive to the application of pathogen screening in practical environments.
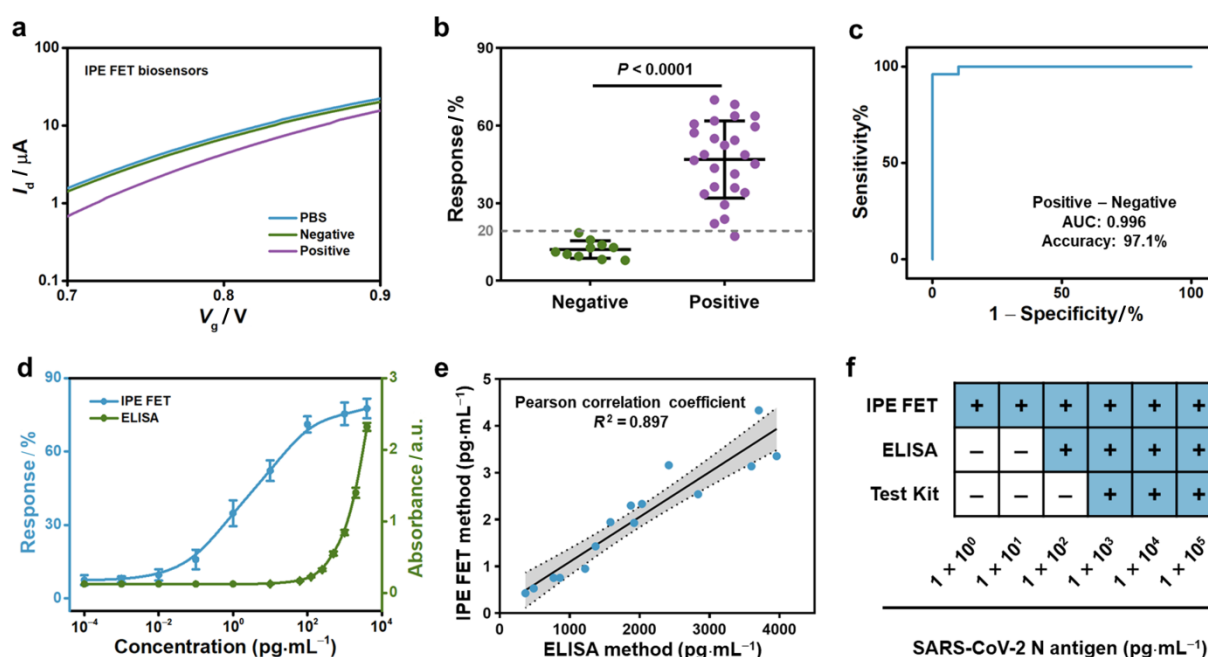
Analysis of SARS-CoV-2 N antigen samples in practical scenarios using IPE FET biosensors

Having demonstrated the excellent performance of the constructed biosensors, PDA-IGZO FET was selected to evaluate the detection ability of IPE FET in practical applications. We first measured the recovery rate of SARS-CoV-2 N antigen by adding a series of concentrations (0.10, 0.50, 1.00, 5.00, and 10.00 pg·mL^{-1}) to negative throat swab samples. The recoveries ranged from 93.0% to 109.5% (Table S1), indicating that IPE FET has great application potential in practical samples. Subsequently, SARS-CoV-2 N antigen was added to negative pharyngeal swab samples to simulate positive pharyngeal swab samples, and the current responses of 25 positive simulated samples and 10 negative samples were tested by IPE FET (Table S2). As depicted in Figure 4a and Figure 4b, the current variations of positive samples are significantly higher than those of negative samples ($P < 0.001$). When 20% current response was selected as the threshold to distinguish negative and positive samples, the discrimination accuracy reached the maximum of 97.1% (95% confidence interval: 84.1%—100.0%). According to the receiver operating characteristic (ROC) curve, the predictive sensitivity and specificity of IPE FET for simulated samples reached 96.0% and 100.0%, respectively (Figure 4c). In addition, the multiple responses toward the same saliva sample are highly consistent (RSD < 5.2%), indicating that IPE FET exhibits good reproducibility in the analysis of saliva samples (Figure S14). These results demonstrate that IPE FET can effectively distinguish the negative and positive samples of the SARS-CoV-2 N antigen in practical scenarios.

Further, we compared the diagnostic ability of IPE FET with ELISA and antigen test kits for simulated samples. Compared with the ELISA kit, which is regarded as the gold standard for quantitative measurement of SARS-CoV-2 N antigen, IPE FET exhibits a lower detection limit and a wider detection range (Figure 4d). Subsequently, we prepared 10 simulated positive samples within the detection range of ELISA, and measured the concentration of SARS-CoV-2 N antigen in each sample by IPE FET after diluting 1000 times (Table S3). According to Pearson's correlation analysis, the results of the two methods showed great linear correlation, indicating that IPE FET has the same detection accuracy as ELISA (Figure 4e). Figure 4f and Figure S15 show the identification results of IPE FETs, ELISA, and antigen test kits on the simulated sample with low-content SARS-CoV-2 N antigen. It can be seen that IPE FET can detect SARS-CoV-2 N antigen in the samples more sensitively. It is worth mentioning that the total detection time of IPE FET for simulated throat swab samples is no more than 5 min, including sampling, incubation, and output of detection results, which is comparable to the N antigen Test Kits (15 min) and much faster than the ELISA technology (about 120 min). IPE FET biosensors also demonstrate promising detection performance compared to previously reported SARS-CoV-2 detection
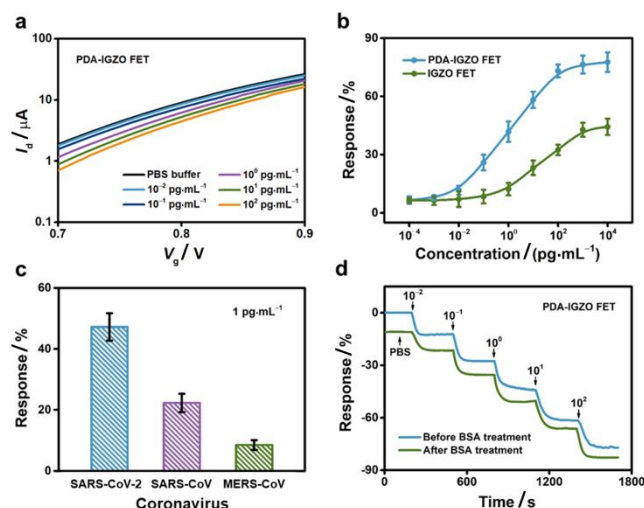
Figure 3 Detection of SARS-CoV-2 N antigens. (a) Transfer characteristic curves of PDA-IGZO FET biosensors toward SARS-CoV-2 N antigen with concentrations ranging from 10^{-2} to 10^2 pg·mL^{-1}. (b) The current responses of IGZO FET and PDA-IGZO FET biosensors as a function of N antigen concentration. (c) Current responses of PDA-IGZO biosensors toward SARS-CoV-2 N antigen, SARS-CoV N antigen, and MERS-CoV N antigen. (d) Real-time response of PDA-IGZO FET biosensors to different concentrations (10^{-2} to 10^2 pg·mL^{-1}) of SARS-CoV-2 N antigen before and after BSA treatment. Data in b and c are reported as mean ± S.D. (n = 3).

Figure 4 Identification of SARS-CoV-2 N antigen in practical scenarios. (a) Transfer characteristic curves of the IPE FET biosensors to negative and positive simulated throat swab samples. (b) Current responses of IPE FET toward SARS-CoV-2 negative and positive samples ($P < 0.05$, unpaired two-sided t-test). The gray line represents the threshold response. (c) ROC curves to predict the detection sensitivity and specificity of IPE FET in SARS-CoV-2 N antigen identifications. AUC: area under curve. (d) The comparison of linear range of IPE FET method with ELISA method. (e) Comparison of the measurement results of IPE FET and ELISA (Pearson correlation coefficient, $R^2 = 0.897$). The shaded grey area denotes the 95% confidence band. (f) The comparison of response performance of IPE FET, ELISA, and Test Kit toward throat swab samples spiked with different concentrations of SARS-CoV-2 N antigen. Data in a are reported as mean ± S.D. ($n = 3$). Data in b and e are reported as mean. ($n = 3$).

assays, including lateral flow immunochromatography, fluorescence immunoassay, and electrical/electrochemical detection assay (Tables S4 and S5). These results indicate that IPE FET can rapidly and accurately detect SARS-CoV-2 N antigen in saliva samples, which offers a promising application prospect in the clinical diagnosis of COVID-19.

Conclusions

In conclusion, we developed an IPE FET to realize highly sensitive and precise detection of SARS-CoV-2 N antigen in practical saliva samples. By modifying polymer layers on the surface of channel material, IPE FET shortened the distance between the target biomolecules and the sensing interface, overcame the limitation of Debye length, and realized ultrasensitive identification of SARS-CoV-2 N antigen in fg·mL^{-1} level. Additionally, the polymer layer effectively reduced the non-specific adsorption of IPE FET and improved the anti-biofouling performance of the biosensor. In a cohort of 35 simulated throat swab samples of SARS-CoV-2 N antigen, IPE FET exhibits an identification accuracy of up to 97.1%, with predictive sensitivity and specificity of 96.0% and 100.0%, respectively. IPE FET could achieve sample-result detection within 5 min and demonstrated quantitative accuracy comparable to ELISA. The excellent performance of IPE FET in the detection of SARS-CoV-2 N antigen not only provides a strategy to design efficient detection platforms but also suggests a pathway to realize rapid and scalable epidemic screening.

Experimental

Chemicals and reagents

Methanol, ethanol, isopropyl alcohol, acetone, glutaraldehyde (25.0%), polyvinyl butyral (PVB), pyrrole (Py), dopamine hydrochloride (DA), sodium *p*-toluenesulfonate, sodium carbonate, and iron(III) chloride (FeCl$_3$, >99.0%) were purchased from Sinopharm

Chemical Reagent Co., Ltd. Poly(methyl methacrylate) (PMMA), trismetyl aminomethane (Tris), and (3-aminopropyl) triethoxysilane (APTES) were obtained from Aladdin. Bovine serum albumin (BSA) and phosphate-buffered saline (PBS) (0.1 mmol/L, 1 mmol/L, and 10 mmol/L, pH 7.4) were bought from Shanghai Yuanye Bio-Technology Co., Ltd. SARS-CoV-2 N antigens were obtained from Wuhan Huamei Biotech Co., Ltd. SARS-CoV antigens, MERS-CoV antigens and the corresponding antibody molecules anti-SARS-CoV-2, anti-SARS-CoV, anti-MERS-CoV were purchased from ACRO Biosystems Co., Ltd.

Instrument and characterization

Ultraviolet (UV) lithography (ABM. Inc, America) and a thermal evaporator system (Jiashuo JSD-300, China) were used to pattern and deposit the metallic electrodes (Cr/Au) array. A radio frequency sputtering system (Jiashuo JSD300-II, China) was used to deposit the IGZO channel layer with the assistance of mask templates. An electron beam lithography system (EBL, JSM-6510, Japan) was used to expose the biosensing region of the FET biosensor. An optical microscope (Olympus BX53MRF-S) was used to obtain the microscopy images of the IGZO biosensing devices. XPS (ESCAI AB250Xi, USA) and ATR-FTIR (FTIR5700, USA) were used to characterize the immobilization of antibody molecules and the modification of PPy on the IGZO surface. High-resolution field-emission SEM (FEI Verios 460, USA) was used to characterize the surface morphology and thickness of the IGZO channel. The digital source meter (Agilent B2902A, USA) was connected to a probe station to measure the electrical characteristics of the IGZO FET device.

Fabrication of IGZO FET arrays

The preparation processes of IGZO FET arrays were as follows.[36] First, the interdigital source, drain, and gate electrodes (15 nm Cr/50 nm Au) were deposited by photolithography and thermal evaporation on a 1 cm × 1 cm Si/SiO$_2$ wafer. With the assistance of a mask template, a 20 nm thick IGZO channel layer was deposited by magnetron sputtering between the patterned

source and drain electrodes. The channel length and width were 500 and 1400 μm, respectively. The Ag/AgCl reference electrodes were firstly fabricated by dropping silver colloidal on the gate electrodes and heating at 75 °C for 15 min to evaporate the solvent, followed by reacting with FeCl$_3$ for 4 min to form an AgCl layer. The surface of Ag/AgCl was then treated with PVB-methanol solution for 3 h at room temperature to form a protective layer.

Electrical characterization of IGZO-FET arrays

The electrical characterization of IGZO-FET arrays was as follows. The transfer characteristic curves were obtained by measuring the relationship between I_d and V_g when V_d is a fixed value. The output characteristic curves were obtained by measuring the relationship between I_d and V_d when V_g is a fixed value. The relationship between V_g and I_d was measured to calculate transconductance (g_m). And the field-effect carrier mobility (μ_{FE}) was calculated using the following equation to evaluate the performance of IGZO-FET:

$$\mu_{FE} = \frac{g_m L}{W V_d C_{ox}} = \frac{dI_d}{dV_g} \frac{L}{W V_d C_{ox}} \tag{2}$$

where L and W are the channel length and width, C_{ox} is capacitance per unit area, and g_m is the transconductance of IGZO-FET.

Construction of IGZO FET biosensors

To achieve the surface functionalization of antibody molecules on the IGZO biosensing channel, a layer of PMMA was spin-coated on the surface of IGZO layer. PMMA eliminated the contact resistance between the source-drain electrode and the biosensing channel as a protective layer to avoid leakage current in the biosensing measurements. Next, the IGZO biosensing region was exposed by electron beam lithography with an area of 500 × 1400 μm^2 and then integrated with a PDMS well (with 2.5 cm length, 1.5 cm width, and 0.3 cm height) for selective functionalization and biosensing. Subsequently, the IGZO surface was covalently functionalized with APTES to introduce amine groups on the IGZO. Specifically, 1 mL of 5% APTES in ethanol was dropped into the PDMS chamber for 1 h and then heated in an oven at 110 °C for 30 min to enhance the silanization of APTES. 1 mL glutaraldehyde (5%) PBS buffer solution was added into the chamber and reacted for 2 h at room temperature to serve as linker molecules. Then, 100 μL antibody solution was added to the IGZO channel and coupled with glutaraldehyde at 4 °C for 12 h. A series of antibody solutions with concentrations ranging from 10—30 μg·mL^{-1} were utilized to explore the optimized antibody modification concentration. To minimize influence of environments such as pH and ion strength on the biosensing performance, the biosensing channels were blocked with BSA (0.01 g·mL^{-1}) at 4 °C for 12 h to minimize the non-specific adsorption.

Construction of IPE FET biosensors

IPE FET biosensors were obtained by modifying PDA/PPy layer on the surface of IGZO FET biosensors. Specifically, the IGZO FET was immersed in 20 mL Tris-HCl buffer solution (50.0 mmol/L, pH = 8.5) containing 0.02 g dopamine, and the PDA layer was prepared by solution polymerization method by shaking at 150 r/min for 20 min, 40 min, 60 min, and 100 min.[37] The PPy layer was prepared by electrochemical deposition at a working voltage of 1.0 V for 30 s, 60 s, 120 s, and 240 s. 20 mL aqueous solution containing 0.15 mol/L Py monomer, 0.1 mol/L sodium *p*-toluenesulfonate, and 0.1 mol/L sodium carbonate was utilized as the PPy precursor solution.[38]

Detection of SARS-CoV-2 N antigens

To achieve the optimized current response, the target N protein incubation time was determined as 5 min before the measurements. The current response of IGZO FET biosensors toward target protein in PBS buffer with different concentrations was recorded to investigate the relationship between ionic strength and the current response of biosensors. The calibrated response curves were recorded by measuring the current responses of the IGZO FET biosensors before and after target N proteins conjugation. The I_d-V_g curves were recorded at V_d = 0.2 V. The I_d-t curves were recorded at V_d = 0.2 V and V_g = 0.7 V. The SARS-CoV N Proteins and MERS-CoV N Proteins with concentrations of 1 pg·mL^{-1} were used as interfering molecules to investigate the selectivity of IPE FET biosensors.

Nonspecific adsorption evaluation of FET biosensors

To evaluate the nonspecific adsorption ability of FET biosensors, PDA-IGZO FET, PPy-IGZO FET, and IGZO FET were immersed in FAM-labeled DNA solution (1 μmol·L^{-1}) and DAPI-stained *E. coli* solution (10^9 cfu·L^{-1}) for 4 h, respectively. The FET biosensors were then removed from the solutions and the adsorption on the surface was observed under a laser confocal microscope.

Simulated throat swab samples preparation and measurements

Negative throat swab samples were collected from the College of Chemistry and Molecular Sciences, Wuhan University. All relevant ethical laws and regulations concerning human participants were complied with. The study was approved by the Ethics Committee of Renmin Hospital of Wuhan University. All the participants in this study signed informed consent forms before participating. The collected negative throat swab samples were stored in VTM at −20 °C.

Simulated throat swab samples were prepared as follows. The SARS-CoV-2 N antigen was diluted in PBS buffer with different concentrations. Then, 10 μL SARS-CoV-2 N antigen solution was added to 90 μL healthy human saliva sample to mimic a SARS-CoV-2 positive saliva sample. Negative samples were nasopharyngeal swab extracts in the absence of antigens. A total of 25 SARS-CoV-2 positive samples and 10 negative simulated throat swab samples were prepared. Each sample (50 μL) was added to the IPE FET biosensors and incubated for 5 min to measure the current responses.

ELISA measurements

Standard solutions and test samples with a range of concentrations diluted with buffer solution were prepared in advance. Sample dilution buffer was used as the control. 100 μL standard, test, and control samples were added into the blank wells and incubated for 90 min at 37 °C. Then, the wells were washed 2 times for 1—2 min each time. 100 μL biotin-labeled antibody solution and 100 μL SABC solution were sequentially added into each well and incubated at 37 °C for 60 min and 30 min, respectively. Each incubation was followed by 3 washing processes. Subsequently, 90 μL TMB substrate solution was added into each well and incubated for 10—20 min at 37 °C. The O.D. absorbance at 450 nm in the Microplate reader was recorded immediately after adding 50 μL stop solution. The relative O.D.450 was calculated as the difference between the O.D.450 of each well and the blank wells. The standard curve was plotted as the relative O.D.450 of each standard solution *versus* the respective concentration of the standard solution. Then, the target concentration of the sample was interpolated from the standard curve.

N antigen Test Kit measurements

Briefly, the sample was mixed with the sample treatment solution. Then, 75—100 μL sample was vertically added into the sample hole of the test card. After 20 min reaction, the test and control lines could be read to determine the result of negative or positive.

Data analysis

All the statistical analysis and the data panels in this article were generated using GraphPad Prism 8 and OriginPro 9. Statisti-

cal details for each experiment can be found in the figure legends.

Supporting Information

Acknowledgement

References

[1] Garcia-Beltran, W. F.; Lam, E. C.; St. Denis, K.; Nitido, A. D.; Garcia, Z. H.; Hauser, B. M.; Feldman, J.; Pavlovic, M. N.; Gregory, D. J.; Poznansky, M. C.; Sigal, A.; Schmidt, A. G.; Iafrate, A. J.; Naranbhai, V.; Balazs, A. B. Multiple SARS-CoV-2 Variants Escape Neutralization by Vaccine-Induced Humoral Immunity. *Cell* **2021**, *184*, 2372–2383.

[2] Harvey, W. T.; Carabelli, A. M.; Jackson, B.; Gupta, R. K.; Thomson, E. C.; Harrison, E. M.; Ludden, C.; Reeve, R.; Rambaut, A.; Peacock, S. J.; Robertson, D. L.; Consortium, C.-G. U. SARS-CoV-2 Variants, Spike Mutations and Immune Escape. *Nat. Rev. Microbiol.* **2021**, *19*, 409–424.

[3] Abdool Karim, S. S.; de Oliveira, T. New SARS-CoV-2 Variants — Clinical, Public Health, and Vaccine Implications. *N. Engl. J. Med.* **2021**, *384*, 1866–1868.

[4] Zhang, T.; Deng, R.; Wang, Y.; Wu, C.; Zhang, K.; Wang, C.; Gong, N.; Ledesma-Amaro, R.; Teng, X.; Yang, C.; Xue, T.; Zhang, Y.; Hu, Y.; He, Q.; Li, W.; Li, J. A paper-Based Assay for the Colorimetric Detection of SARS-CoV-2 Variants at Single-Nucleotide Resolution. *Nat. Biomed. Eng.* **2022**, *6*, 957–967.

[5] Arizti-Sanz, J.; Bradley, A. D.; Zhang, Y. B.; Boehm, C. K.; Freije, C. A.; Grunberg, M. E.; Kosoko-Thoroddsen, T.-S. F.; Welch, N. L.; Pillai, P. P.; Mantena, S.; Kim, G.; Uwanibe, J. N.; John, O. G.; Eromon, P. E.; Kocher, G.; Gross, R.; Lee, J. S.; Hensley, L. E.; MacInnis, B. L.; Johnson, J.; Springer, M.; Happi, C. T.; Sabeti, P. C.; Myhrvold, C. Simplified Cas13-Based Assays for the Fast Identification of SARS-CoV-2 and its Variants. *Nat. Biomed. Eng.* **2022**, *6*, 932–943.

[6] Nguyen, L. T.; Rananaware, S. R.; Pizzano, B. L. M.; Stone, B. T.; Jain, P. K. Clinical Validation of Engineered CRISPR/Cas12a for Rapid SARS-CoV-2 Detection. *Commun. Med.* **2022**, *2*, 7.

[7] Leonard, E. K.; Aller Pellitero, M.; Juelg, B.; Spangler, J. B.; Arroyo-Currás, N. Antibody–Invertase Fusion Protein Enables Quantitative Detection of SARS-CoV-2 Antibodies Using Widely Available Glucometers. *J. Am. Chem. Soc.* **2022**, *144*, 11226–11237.

[8] Baker, A. N.; Richards, S.-J.; Guy, C. S.; Congdon, T. R.; Hasan, M.; Zwetsloot, A. J.; Gallo, A.; Lewandowski, J. R.; Stansfeld, P. J.; Straube, A.; Walker, M.; Chessa, S.; Pergolizzi, G.; Dedola, S.; Field, R. A.; Gibson, M. I. The SARS-COV-2 Spike Protein Binds Sialic Acids and Enables Rapid Detection in a Lateral Flow Point of Care Diagnostic Device. *ACS Cent. Sci.* **2020**, *6*, 2046–2052.

[9] Shao, W.; Shurin, M. R.; Wheeler, S. E.; He, X.; Star, A. Rapid Detection of SARS-CoV-2 Antigens Using High-Purity Semiconducting Single-Walled Carbon Nanotube-Based Field-Effect Transistors. *ACS Appl. Mater. Interfaces* **2021**, *13*, 10321–10327.

[10] Ahmed, R.; Guimarães, C. F.; Wang, J.; Soto, F.; Karim, A. H.; Zhang, Z.; Reis, R. L.; Akin, D.; Paulmurugan, R.; Demirci, U. Large-Scale Functionalized Metasurface-Based SARS-CoV-2 Detection and Quantification. *ACS Nano* **2022**, *16*, 15946–15958.

[11] Yao, L.; Zhu, W.; Shi, J.; Xu, T.; Qu, G.; Zhou, W.; Yu, X.-F.; Zhang, X.; Jiang, G. Detection of Coronavirus in Environmental Surveillance and Risk Monitoring for Pandemic Control. *Chem. Soc. Rev.* **2021**, *50*, 3656–3676.

[12] Sethuraman, N.; Jeremiah, S. S.; Ryo, A. Interpreting Diagnostic Tests for SARS-CoV-2. *JAMA* **2020**, *323*, 2249–2251.

[13] Lee, J.-H.; Choi, M.; Jung, Y.; Lee, S. K.; Lee, C.-S.; Kim, J.; Kim, J.; Kim, N. H.; Kim, B.-T.; Kim, H. G. A Novel Rapid Detection for SARS-CoV-2 Spike 1 Antigens Using Human Angiotensin Converting Enzyme 2 (ACE2). *Biosens. Bioelectron.* **2021**, *171*, 112715.

[14] Yamaoka, Y.; Miyakawa, K.; Jeremiah, S. S.; Funabashi, R.; Okudela, K.; Kikuchi, S.; Katada, J.; Wada, A.; Takei, T.; Nishi, M.; Shimizu, K.; Ozawa, H.; Usuku, S.; Kawakami, C.; Tanaka, N.; Morita, T.; Hayashi, H.; Mitsui, H.; Suzuki, K.; Aizawa, D.; Yoshimura, Y.; Miyazaki, T.; Yamazaki, E.; Suzuki, T.; Kimura, H.; Shimizu, H.; Okabe, N.; Hasegawa, H.; Ryo, A. Highly Specific Monoclonal Antibodies and Epitope Identification Against SARS-CoV-2 Nucleocapsid Protein for Antigen Detection Tests. *Cell Rep. Med.* **2021**, *2*, 100311.

[15] Wang, C.; Cheng, X.; Liu, L.; Zhang, X.; Yang, X.; Zheng, S.; Rong, Z.; Wang, S. Ultrasensitive and Simultaneous Detection of Two Specific SARS-CoV-2 Antigens in Human Specimens Using Direct/Enrichment Dual-Mode Fluorescence Lateral Flow Immunoassay. *ACS Appl. Mater. Interfaces* **2021**, *13*, 40342–40353.

[16] Guo, Y. N.; Tao, J.; Li, Y. R.; Feng, Y. M.; Ju, H. X.; Wang, Z. F.; Ding, L. Quantitative Localized Analysis Reveals Distinct Exosomal Protein-Specific Glycosignatures: Implications in Cancer Cell Subtyping, Exosome Biogenesis, and Function. *J. Am. Chem. Soc.* **2020**, *142*, 7404–7412.

[17] Wu, N.; Bao, L.; Ding, L.; Ju, H. A Single Excitation-Duplexed Imaging Strategy for Profiling Cell Surface Protein-Specific Glycoforms. *Angew. Chem. Int. Ed.* **2016**, *55*, 5220–5224.

[18] Zhang, Z.; Pandey, R.; Li, J.; Gu, J.; White, D.; Stacey, H. D.; Ang, J. C.; Steinberg, C.-J.; Capretta, A.; Filipe, C. D. M.; Mossman, K.; Balion, C.; Miller, M. S.; Salena, B. J.; Yamamura, D.; Soleymani, L.; Brennan, J. D.; Li, Y. High-Affinity Dimeric Aptamers Enable the Rapid Electrochemical Detection of Wild-Type and B.1.1.7 SARS-CoV-2 in Unprocessed Saliva. *Angew. Chem. Int. Ed.* **2021**, *60*, 24266–24274.

[19] Siavash Moakhar, R.; del Real Mata, C.; Jalali, M.; Shafique, H.; Sanati, A.; de Vries, J.; Strauss, J.; AbdElFatah, T.; Ghasemi, F.; McLean, M.; Hosseini, I.; Lu, Y.; Yedire, S. G.; Mahshid, S. S.; Tabatabaiefar, M. A.; Liang, C.; Mahshid, S. A Versatile Biomimic Nanotemplating Fluidic Assay for Multiplex Quantitative Monitoring of Viral Respiratory Infections and Immune Responses in Saliva and Blood. *Adv. Sci.* **2022**, *9*, 2204246.

[20] Dai, C.; Liu, Y.; Wei, D. Two-Dimensional Field-Effect Transistor Sensors: The Road Toward Commercialization. *Chem. Rev.* **2022**, *122*, 10319–10392.

[21] Sadighbayan, D.; Hasanzadeh, M.; Ghafar-Zadeh, E. Biosensing Based on Field-Effect Transistors (FET): Recent Progress and Challenges. *TrAC, Trends Anal. Chem.* **2020**, *133*, 116067.

[22] Song, J.; Liu, H.; Zhao, Z.; Lin, P.; Yan, F. Flexible Organic Transistors for Biosensing: Devices and Applications. *Adv. Mater.* Accepted Author Manuscript 2300034. https://doi.org/10.1002/adma.202300034.

[23] Kaisti, M., Detection Principles of Biological and Chemical FET Sensors. *Biosens. Bioelectron.* **2017**, *98*, 437–448.

[24] Kang, H.; Wang, X.; Guo, M.; Dai, C.; Chen, R.; Yang, L.; Wu, Y.; Ying, T.; Zhu, Z.; Wei, D.; Liu, Y.; Wei, D. Ultrasensitive Detection of SARS-CoV-2 Antibody by Graphene Field-Effect Transistors. *Nano Lett.* **2021**, *21*, 7897–7904.

[25] Chen, M.; Cui, D.; Zhao, Z.; Kang, D.; Zhen, L.; Albawardi, S.; Alsageer, S.; Alamri, S.; Alhazmi, A.; Amer, M. R.; Zhou, C. Highly sensitive, scalable, and rapid SARS-CoV-2 biosensor based on In$_2$O$_3$ nanoribbon transistors and phosphatase. *Nano Res.* **2022**, *15*, 5510–5516.

[26] Dai, C.; Guo, M.; Wu, Y.; Cao, B.-P.; Wang, X.; Wu, Y.; Kang, H.; Kong, D.; Zhu, Z.; Ying, T.; Liu, Y.; Wei, D. Ultraprecise Antigen 10-in-1 Pool Testing by Multiantibodies Transistor Assay. *J. Am. Chem. Soc.* **2021**, *143*, 19794–19801.

[27] Yang, Y.; Wang, J.; Huang, W.; Wan, G.; Xia, M.; Chen, D.; Zhang, Y.; Wang, Y.; Guo, F.; Tan, J.; Liang, H.; Du, B.; Yu, L.; Tan, W.; Duan, X.; Yuan, Q. Integrated Urinalysis Devices Based on Interface-Engineered

Field-Effect Transistor Biosensors Incorporated with Electronic Circuits. *Adv. Mater.* **2022**, *34*, 2203224.

[28] Shao, W.; Shuin, M. R.; Wheeler, S. E.; He, X.; Star, A. Rapid Detection of SARS-CoV-2 Antigens Using High-Purity Semiconducting Single-Walled Carbon Nanotube-Based Field-Effect Transistors. *ACS Appl. Mater. Interfaces* **2021**, *13*, 10321–10327.

[29] Nakatsuka, N.; Yang, K.-A.; Abendroth, J. M.; Cheung, K. M.; Xu, X.; Yang, H.; Zhao, C.; Zhu, B.; Rim, Y. S.; Yang, Y.; Weiss, P. S.; Stojanović, M. N.; Andrews, A. M. Aptamer-Field-Effect Transistors Overcome Debye Length Limitations for Small-Molecule Sensing. *Science* **2018**, *362*, 319–324.

[30] Vacic, A.; Criscione, J. M.; Rajan, N. K.; Stern, E.; Fahmy, T. M.; Reed, M. A. Determination of Molecular Configuration by Debye Length Modulation. *J. Am. Chem. Soc.* **2011**, *133*, 13886–13889.

[31] Zheng, Z.; Zhang, H.; Zhai, T.; Xia, F. Overcome Debye Length Limitations for Biomolecule Sensing Based on Field Effective Transistors. *Chin. J. Chem.* **2021**, *39*, 999–1008.

[32] Zhang, Y.; Wang F.; Zhang H.; Wang, H.; Liu, Y. Multivalency Interface and g-C$_3$N$_4$ Coated Liquid Metal Nanoprobe Signal Amplification for Sensitive Electrogenerated Chemiluminescence Detection of Exosomes and Their Surface Proteins. *Anal. Chem.* **2019**, *91*, 12100–12107.

[33] Zhang, H.; Wang Z.; Wang, F.; Zhang, Y.; Wang, H.; Yang, L. In Situ Formation of Gold Nanoparticles Decorated Ti$_3$C$_2$ MXenes Nanoprobe for Highly Sensitive Electrogenerated Chemiluminescence Detection of Exosomes and Their Surface Proteins. *Anal. Chem.* **2020**, *92*, 5546–5553.

[34] Yun, S. H.; Ingole, P. G.; Kim, K. H.; Choi, W. K.; Kim, J. H.; Lee, H. K. Properties and Performances of Polymer Composite Membranes Correlated with Monomer and Polydopamine for Flue Gas Dehydration by Water Vapor Permeation. *Chem. Eng. J.* **2014**, *258*, 348–356.

[35] Romero, I. S.; Schurr, M. L.; Lally, J. V.; Kotlik, M. Z.; Murphy, A. R. Enhancing the Interface in Silk–Polypyrrole Composites through Chemical Modification of Silk Fibroin. *ACS Appl. Mater. Interfaces* **2013**, *5*, 553–564.

[36] Guo, J.; Shen, R.; Shen, X.; Zeng, B.; Yang, N.; Liang, H.; Yang, Y.; Yuan, Q. Construction of High Stability Indium Gallium Zinc Oxide Transistor Biosensors for Reliable Detection of Bladder Cancer-Associated MicroRNA. *Chin. Chem. Lett.* **2022**, *33*, 979–982.

[37] Wang, H.; Lin, Q.; Yin, L.; Yang, Y.; Qiu, Y.; Lu, C.; Yang, H. Biomimetic Design of Hollow Flower-Like g-C$_3$N$_4$@PDA Organic Framework Nanospheres for Realizing an Efficient Photoreactivity. *Small* **2019**, *15*, 1900011.

[38] Cao, P.; Wang, N.; Dai, H.; Ma, H.; Lin, M. Molybdenum-Containing Polypyrrole Self-Supporting Hollow Flexible Electrode for Hydrogen Peroxide Detection in Living Cells. *Anal. Chim. Acta* **2021**, *1151*, 338251.
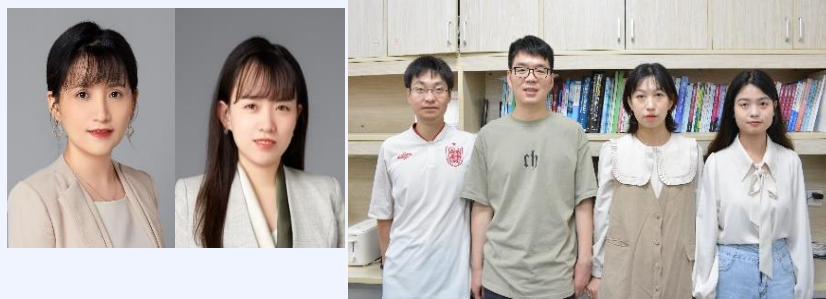
The Authors

Left to Right: Quan Yuan, Yanbing Yang, Duo Chen, Zhipeng Gao, Wanting Huang, Qiumin Peng